AD-A049 113 NAVAL RESEARCH LAB WASHINGTON D C F/G 20/12
GENERATION OF INTERMODULATION BY ELECTRON TUNNELING THROUGH ALU--ETC(U)
OCT 77 C D BOND, C S GUENZER, C A CAROSELLA

UNCLASSIFIED NRL-8170 SBIE-AD-E000 062 NL

| OF |
AD
A049113

END
DATE
FILMED
3-78
DDC

NRL Report 8170

Generation of Intermodulation by Electron Tunneling through Aluminum Oxide Films

C. D. BOND, C. S. GUENZER, and C. A. CAROSELLA

Radiation Effects Branch
Radiation Technology Division

October 26, 1977

NAVAL RESEARCH LABORATORY
Washington, D.C.

(14) NRL-8170

(9) Final rept.,

SECURITY CLASSIFICATION OF THIS PAGE (When Data Entered)

REPORT DOCUMENTATION PAGE

READ INSTRUCTIONS BEFORE COMPLETING FORM

1. REPORT NUMBER: NRL Report 8170
2. GOVT ACCESSION NO.
3. RECIPIENT'S CATALOG NUMBER

(6) 4. TITLE (and Subtitle): GENERATION OF INTERMODULATION BY ELECTRON TUNNELING THROUGH ALUMINUM OXIDE FILMS

5. TYPE OF REPORT & PERIOD COVERED: Final Report on the NRL Problem
6. PERFORMING ORG. REPORT NUMBER

(10) 7. AUTHOR(s): C. D. Bond, C. S. Guenzer, C. A. Carosella

8. CONTRACT OR GRANT NUMBER(s): (16) RDF 73

9. PERFORMING ORGANIZATION NAME AND ADDRESS: Naval Research Laboratory, Washington, D.C. 20375

10. PROGRAM ELEMENT, PROJECT, TASK AREA & WORK UNIT NUMBERS: NRL ~~Problem~~ R08-73, Program Element 33109N, Project ~~XCC~~-46

11. CONTROLLING OFFICE NAME AND ADDRESS: Naval Electronic Systems Command, Washington, D.C. 20360

12. REPORT DATE: October 26, 1977
13. NUMBER OF PAGES: ~~29~~

14. MONITORING AGENCY NAME & ~~ADDRESS(if different from Controlling Office)~~: (11) 26 Oct 77

15. SECURITY CLASS. (of this report): UNCLASSIFIED
15a. DECLASSIFICATION/DOWNGRADING SCHEDULE

16. DISTRIBUTION STATEMENT (of this Report): Approved for public release; distribution unlimited

(12) 29p.

DDC RECEIVED JAN 31 1978 B

17. DISTRIBUTION STATEMENT (of the abstract entered in Block 20, if different from Report)

(18) SBIE

(19) AD-E000 062

18. SUPPLEMENTARY NOTES

19. KEY WORDS (Continue on reverse side if necessary and identify by block number)

Satellite communication	Junction circuit analysis
Intermodulation interference	Current-voltage characteristics
Nonlinear conduction	Capacitance characteristics
Tunneling junctions	Time characteristics
Junction fabrication	Junction ion implantation

20. ABSTRACT (Continue on reverse side if necessary and identify by block number)

In the Navy's Fleet Satellite Communication System (FLTSATCOM) the existence of nonlinear conduction mechanisms in passive hardware components has resulted in the generation of intermodulation (frequency mixing) which degrades the system performance. Consequently there is an urgent need for a systematic investigation of the basic mechanisms that can produce intermodulation.

This report describes an investigation of the generation of RF intermodulation due to nonlinear conduction by electron tunneling through thin-film aluminum oxide junctions. Details are presented

over

(Continued)

DD FORM 1 JAN 73 1473 EDITION OF 1 NOV 65 IS OBSOLETE S/N 0102-014-6601

SECURITY CLASSIFICATION OF THIS PAGE (When Data Entered)

251 950 B

20. Abstract (Continued)

regarding the fabrication of junctions, their current-voltage characteristics, and the measurement of intermodulation power levels. The measured ratio of intermodulation power to signal power was 10^{-15} to 10^{-11}, which is significantly higher than the desired 10^{-19}. The measured intermodulation levels are correlated with the device circuit parameters and with existing tunneling theory. In addition the report describes some preliminary results of efforts to improve the conduction characteristics of such junctions by ion implantation. Initial implantation results with silver atoms are sufficiently promising to warrant further investigation with different atoms, greater implantation depths, and higher fluences.

CONTENTS

INTRODUCTION 1

TUNNELING THEORY 4

JUNCTION FABRICATION 6

CURRENT-VOLTAGE CHARACTERISTICS 7

CAPACITANCE MEASUREMENTS 12

INTERMODULATION MEASUREMENTS 13

ION IMPLANTATION EFFECTS 21

CONCLUSIONS 23

ACKNOWLEDGMENTS 24

REFERENCES 24

GENERATION OF INTERMODULATION BY ELECTRON TUNNELING THROUGH ALUMINUM OXIDE FILMS

INTRODUCTION

The Navy's Fleet Satellite Communication System (FLTSATCOM) consists basically of three synchronous-orbit satellites with UHF links to various earth-surface terminals. Each satellite and surface terminal simultaneously operates both transmitter and receiver units in close physical proximity. The Navy's transmit and receive bands are approximately 240 to 270 MHz and 290 to 320 MHz respectively. These two carrier bands are separated by only 20 MHz. For such a system to operate successfully, any undesirable frequency mixing caused by nonlinear components (intermodulation (IM) generation) must be minimized.

The severe magnitude of this problem can best be illustrated by calculating the acceptable IM power level at a receiver for typical operating conditions; for example, for a satellite transmitter power of ≈ 100 W (+50 dBm) the space attenuation alone is ≈ 175 dB (- 125 dBm, or down to 3×10^{-16} W) for either the uplink or downlink signals. At the satellite receiver the uplink signals should normally be ≈ 15 dB above any interference or noise level. This requires the interference level to be below -140 dBm, or 10^{-17} W. Thus the acceptable IM level at the satellite receiver is required to be 190 dB below the local transmitted power level. This is a ratio of IM power to signal power of 10^{-19}. The same requirement must also be met at the earth-based terminals.

This problem is diagramed in Fig. 1 by an illustration from Young [1]. Here the IM products are presented in a simplified two-signal analysis. Consider two frequencies f_1 and f_2 in the transmit band at voltage levels of V_1 and V_2. The input voltage V_{in} across some network can be written

$$V_{in} = V_1 \cos \omega_1 t + V_2 \cos \omega_2 t. \tag{1}$$

For a linear network the output current will be

$$I = G_0 V_{in}.$$

For a nonlinear network the output current can be expressed as the power series

$$I = G_0 V_{in} + G_1 V_{in}^2 + G_2 V_{in}^3 + \dots . \tag{2}$$

Manuscript submitted September 12, 1977.

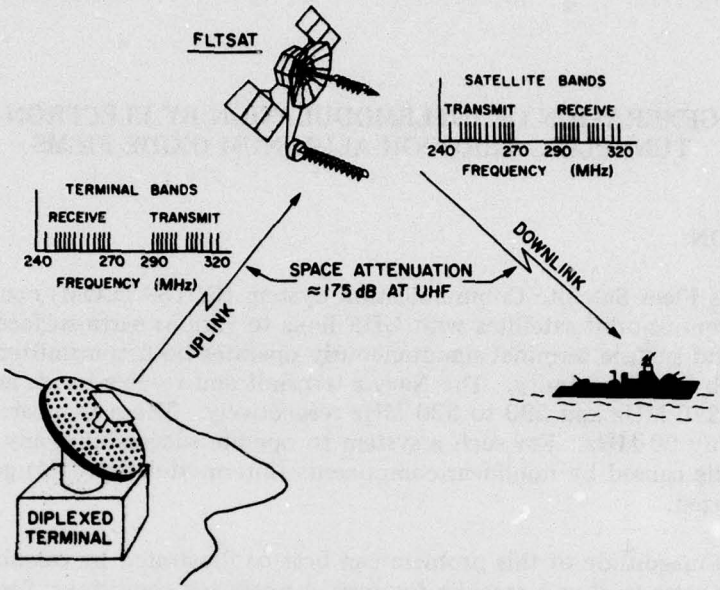

(a) Basic satellite communication system

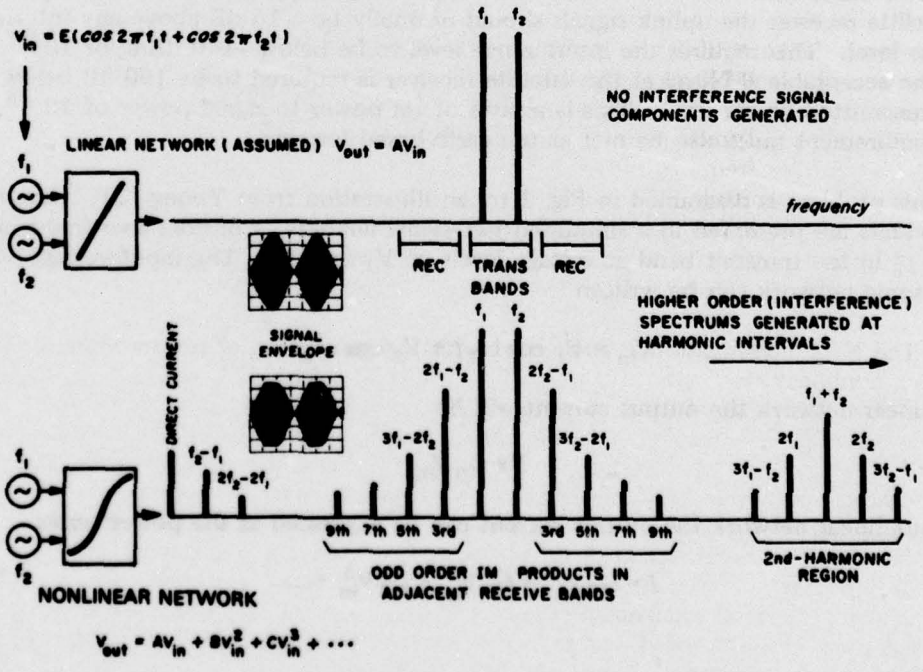

(b) Simplified two-signal analysis

Fig. 1 — Basic satellite communication system showing simplified two-signal analysis for a linear and a nonlinear network. The intermodulation-frequency terms result from a power series representation of the nonlinear signal-voltage output and constitute interference in the receive bands.

The separate IM term in the nonlinear output can be seen by substituting the input voltage of Eq. (1) into Eq. (2) to give

$$
\begin{aligned}
I = {} & G_0(V_1 \cos \omega_1 t + V_2 \cos \omega_2 t) + \\
& G_1 \left[\frac{V_1^2 + V_2^2}{2} + \frac{1}{2} V_1^2 \cos 2\omega_1 t + \frac{1}{2} V_2^2 \cos 2\omega_2 t \right. \\
& \left. + V_1 V_2 \cos (\omega_1 - \omega_2) + V_1 V_2 \cos (\omega_1 + \omega_2) \right] + \\
& G_2 \left[\frac{1}{4} V_1^3 \cos 3\omega_1 t + \frac{1}{4} V_2^3 \cos 3\omega_2 t + 3V_1 \left(\frac{V_2^2}{2} + \frac{V_1^2}{4} \right) \cos \omega_1 t \right. \\
& + 3V_2 \left(\frac{V_1^2}{2} + \frac{V_2^2}{4} \right) \cos \omega_2 t + \frac{3}{4} V_1 V_2^2 \cos (2\omega_2 - \omega_1) t \\
& + \frac{3}{4} V_1 V_2^2 \cos (2\omega_2 + \omega_1) + \frac{3}{4} V_1^2 V_2 \cos (2\omega_1 - \omega_2) \\
& \left. + \frac{3}{4} V_1^2 V_2 \cos (2\omega_1 + \omega_2) \right] + \ldots . \qquad (3)
\end{aligned}
$$

The frequencies f_1 = 250 MHz and f_2 = 270 MHz have been chosen for most of the device testing at the NRL IM test facility.

At these two typical satellite transmitter frequencies, most of the IM terms shown in Eq. (3) include frequencies that lie outside the satellite receive band. However, two of the largest magnitude IM terms of frequencies $2f_2 - f_1$ and $3f_2 - 2f_1$ (290 MHz and 310 MHz) do fall within the local receive band. (The source of the latter IM frequency is the V^5 term and is not shown in Eq. (3).) This example illustrates the problem resulting from a narrow separation of the transmit-receive bands.

The NRL investigation is concerned with the generation of intermodulation due to various nonlinear mechanisms in normally passive hardware such as contacts, flanges, connectors, and other current-carrying metal structures attendant to the transmitter-receiver system. The investigation described in this report is specifically concerned with the generation of intermodulation due to the nonlinear conduction by electrons tunneling through thin oxide films, particularly Al_2O_3 on aluminum structures.

The detailed mechanisms of surface-to-surface contacts is extremely involved and complex and remains incompletely understood. There are many interacting variables, such as the density of microscopic contact points, number of contacts, contact pressure, oxide growth, oxide fracture and regrowth, metal-to-metal bonding, diffusion, and time and temperature effects.

Despite the lack of a complete microscopic theory, contact models such as those described in the Philco-Ford report [2] do allow predictions adequate for assessment and control of the intermodulation generated in real hardware contacts. Because of the

numerous contact mechanisms which have been identified, an experimental study of tunneling in real contacts is not amenable to reproducible results and to correlation with theory [3]. Consequently the intent of this experimental investigation is to fabricate well-characterized tunneling junctions of Al-Al_2O_3-Al, to directly measure the intermodulation generated, and to attempt to correlate the intermodulation with the device circuit parameters and with tunneling theory. In addition some preliminary efforts were made to improve the conduction characteristics of such junctions by ion implantation.

TUNNELING THEORY

The theory of electron tunneling through an insulating layer dates back to the 1920's. However controversy still continues as to the correct form of the tunneling equations for thin films ($\lesssim 5$ nm). Some of the principal difficulties include the following:

- Applicability of macroscopic parameters, such as the dielectric constant, to a few atomic layers,

- Complexity of integrals which can presently be solved only by approximations which affect the accuracy of the final results to an undetermined degree, and

- *Accurate evaluation of contaminant effects on the electron scattering surfaces.*

This last effect has been developed into a valuable qualitative method for investigating the vibrational modes of the contaminants, but quantitatively the effect is poorly understood. Thus comparison of the experimental results with the electron tunneling theory is only approximately quantitative.

The theory of electron tunneling is based on the fact that the wave function of a free electron ψ_e extends only a few nanometers into an insulator at any metal-insulator interface. In large-dimension insulators the wave function quickly decreases to a vanishingly small value such that the effect goes unnoticed; but if the insulator is only 3 nm (a typical aluminum oxide film), the wave function ψ_e remains finite throughout the insulator and yields a measurable probability for the electron to pass from one side of the insulator to the other. This effect is shown in Fig. 2, where the extended wave function ψ_e on the left is matched in magnitude and slope to the decaying exponential within the insulator, which, before it vanishes, similarly matches with the extended wave function in the metal on the right.

Since temperature has a small effect, one needs only the zero-temperature expression for the tunneling current density J in one direction [4]:

$$J = \frac{me}{2\pi^2\hbar^3}\left[eV\int_0^{E_{F_1}-eV} P(E)\,dE + \int_{E_{F_1}-eV}^{E_{F_1}} (E_{F_1} - E)P(E)\,dE\right].$$

The parameters are shown in Fig. 2, where V is the voltage applied across the junction and E_{F_1} is the Fermi level of the electron distribution in the metal on the left. $P(E)$ is the transmission probability by tunneling for electrons of transverse energy E.

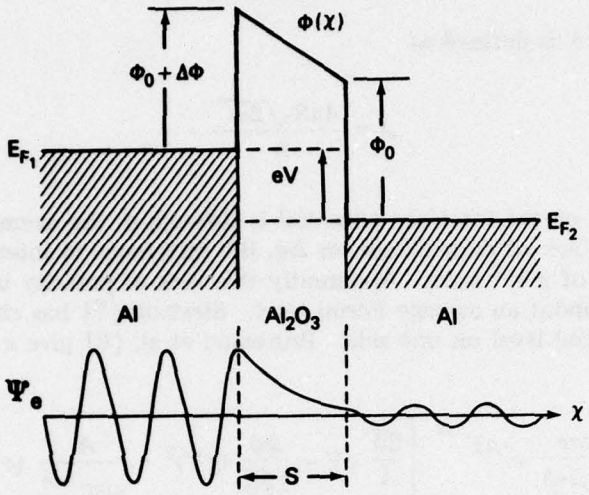

Fig. 2 — Electron tunneling through the potential barrier of a thin insulating film between two conductors. The conductors of the sandwich structure are maintained at a potential difference of V such that there is a finite electron probability function ψ_e everywhere to the right of the first interface. The resulting current is a nonlinear function of voltage.

The usual method for calculating the transmission probability involves the WKB approximation, which yields a transmission probability given by

$$P(E) = \exp\left[-2\int_S \sqrt{\frac{2m}{\hbar^2}\,[\phi(x) - e]}\,dx\right].$$

In this expression, $\phi(x)$ is the local barrier potential acting on the electron within the classically forbidden region of the aluminum oxide, and the integral is carried out over the width of the forbidden region S. For the simple trapezoidal barrier shown in Fig. 2, the transmission probability from left to right is given exactly by

$$P(E) = \exp\left\{-\frac{4}{3}\,\frac{2m}{\hbar}\left(\frac{S}{eV + \Delta\phi}\right)\left[(E + \phi_0 + eV + \Delta\phi)^{3/2} - (E + \phi_0)^{3/2}\right]\right\}.$$

This exponential expression is sufficiently complex so that the last integral in the initial equation for J cannot be carried out exactly. Forlani and Minnaja [5] have expanded the argument of the exponential about the average of the Fermi levels and obtained an approximate analytical expression for the tunneling current density J. As part of this investigation a Taylor expansion of the Forlani-Minnaja equation to the fourth order in voltage has been published [6]:

$$J = \frac{me}{2\pi^2\hbar^3}\,e^{-A\bar{\phi}^{1/2}}\left[\left(\frac{2\bar{\phi}^{1/2}}{A} + \frac{2}{A^2}\right)eV + \frac{A}{48\bar{\phi}^{1/2}}\,(eV)^3\right], \tag{4}$$

where the parameter A is defined as

$$A = \frac{4\pi S\sqrt{2m}}{\hbar} .$$

The dependence on the interface potential is through $\overline{\phi}$, the average of the two interface potentials. The lack of dependence on $\Delta\phi$, the difference in interface potentials, is reflected by the lack of a V^2 term. Apparently this lack of polarity is caused by the choice of expansion about an average Fermi level. Stratton [7] has chosen instead to expand about the Fermi level on one side. Brinkman et al. [8] give a low-voltage expansion for this case as

$$J = \frac{me}{2\pi^2\hbar^3}\, e^{-A\overline{\phi}^{1/2}} \left[\frac{2\overline{\phi}}{A}\, eV - \frac{\Delta\phi}{12\overline{\phi}}\, (eV)^2 + \frac{A}{16\overline{\phi}^{1/2}}\, (eV)^3\right],$$

where

$$\overline{\phi} = \phi_0 + \frac{1}{2}\,\Delta\phi.$$

Here, not only is the cubic term 3 times larger than in Eq. (4), but there is a significant quadratic term proportional to $\Delta\phi$. Unfortunately this expression is only approximate, and Brinkman et al. do not state the approximations involved. Thus the simplest type of theory is somewhat uncertain even for the second- and third-order terms.

JUNCTION FABRICATION

The laboratory fabrication of an electron tunneling junction is illustrated in Fig. 3. The procedure involves the vacuum evaporation of an aluminum strip $\approx$150 nm thick onto a clean glass substrate. The strip is then allowed to oxidize at room temperature from 12 to 24 hours. Following this oxidation a second similar strip is deposited at right angles to the first strip. The resulting junction sandwich area consist of two parallel plates of thin aluminum separated by an aluminum oxide insulating film approximately 3 nm thick. Such a structure serves as a useful tool in the experimental study of the electron tunneling phenomena described in the previous section.

In practice, five to ten such junctions were usually fabricated simultaneously under the same conditions to establish controls and statistics. The vacuum-chamber arrangement for evaporation, masking, and monitoring is shown in Fig. 4. Prior to evaporation a Vac-Ion pump is used to evacuate the chamber to a pressure of $\lesssim 5 \times 10^{-7}$ torr. After degassing the tungsten basket filament and its aluminum contents (0.5 g of 99.999+% aluminum), the aluminum is evaporated rapidly in $\lesssim$1.0 minute. During the evaporation the chamber pressure typically increases to $\lesssim 8 \times 10^{-6}$ torr. A shutter arrangement is used to control the starting and stopping of aluminum deposition. (The circular shutter is displaced to the left in Fig. 4.) The film thickness is monitored during evaporation both by measuring the film resistance and by a direct-reading digital monitor of the crystal oscillator type (Sloan 200). The programmable monitor is also used to follow

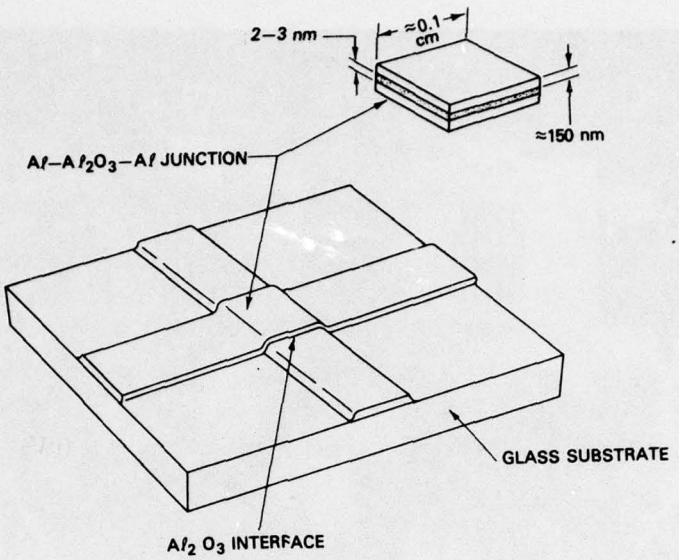

Fig. 3 — Laboratory technique used in fabricating tunneling-junction sandwich structures of Al-Al_2O_3-Al. The aluminum oxide film is grown at room temperature on a vacuum-evaporated aluminum strip and overlayed with a second aluminum strip as shown.

directly the subsequent growth of the aluminum oxide. After the aluminum film evaporation, the monitor is reset to zero thickness, and the density of Al_2O_3 is dialed into the monitor. After the pressure in the chamber is increased to 1 atmosphere of pure oxygen, the Al_2O_3 thickness increases from zero to $\approx$2 nm in the first 5 minutes and then grows more slowly, reaching 2.2 to 2.7 nm after about 1 hour. Although no oxide growth was ever observed in this study after a few hours, the second evaporation of aluminum over the oxide growth was not carried out until 12 to 24 hours later.

Figure 5 shows a typical assembly of five junctions at three stages of fabrication. Initially thin strips of indium are "soldered" onto the glass microscope slide to form electrical contacts. (Molten indium readily adheres to a clean glass surface.) A mask is carefully aligned over the contacts, and a strip of aluminum is evaporated onto the glass and indium contacts. After the strip is oxidized, a set of five aluminum-film strips are similarly evaporated simultaneously at right angles to the first strip. Finally No. 36 copper magnet-wire leads are soldered onto the indium contacts.

CURRENT-VOLTAGE CHARACTERISTICS

The electrical properties of these junctions which are of primary interest in this application are their nonlinear resistance characteristics and their generation of RF intermodulation. The nonlinear DC current-voltage (I-V) characteristics of such junctions were measured with a standard four-point arrangement (Fig. 6). A programmable constant-current supply (Keithley 227) is used to drive from 3 nA to 1 mA through two legs of the junction film leads. A 5-1/2-digit digital voltmeter is used to measure the voltage

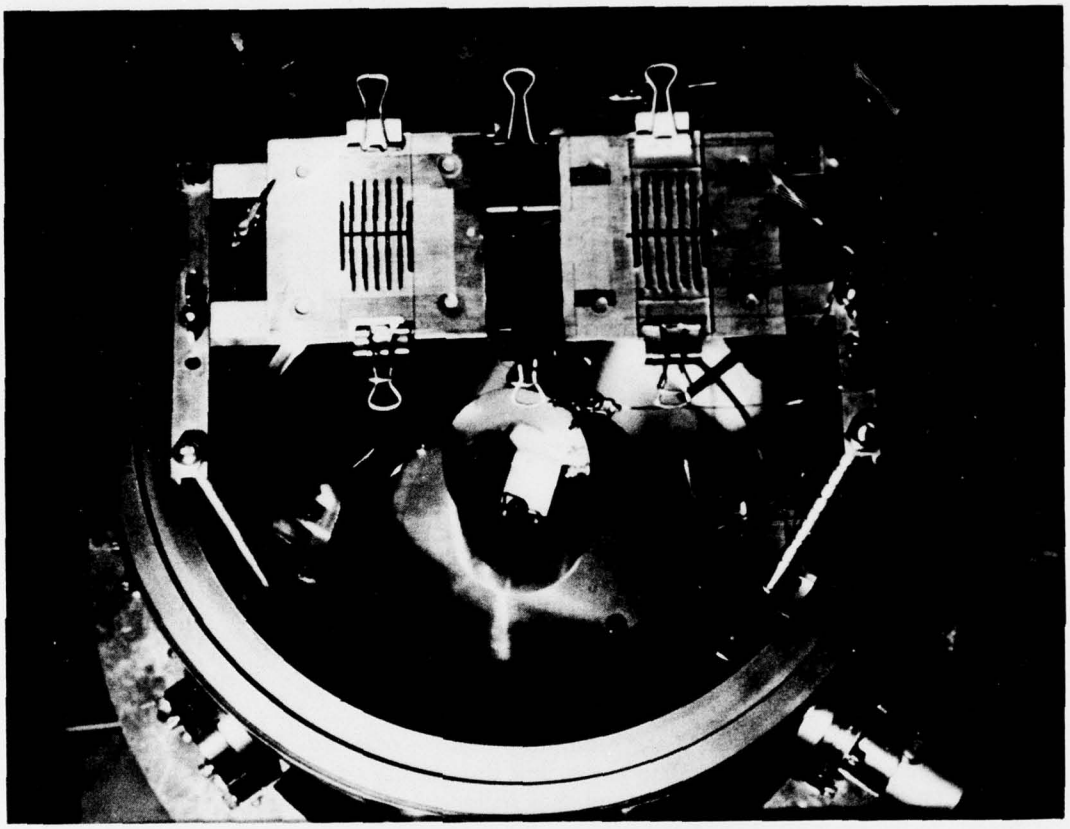

Fig. 4 — Vacuum-chamber arrangement for evaporation, masking, and monitoring. The crystal head of the Sloan thickness monitor is normally mounted in the plane of the substrate surfaces and is not shown in this photograph.

developed across the junction. Since the input impedance of the voltmeter is $>10^8$ ohms, negligible current from the current source flows through the voltmeter circuit, and the effects of lead resistance and contact resistance are essentially eliminated; that is, the only IR drop seen by the voltmeter is across the junction area. The current is measured by a digital multimeter (Keithley 164).

Figure 7 shows the current-voltage characteristic curve for one of the early 0.0168-cm^2 devices. On the scale shown the experimental curve becomes visibly nonlinear at about 80 mV and exhibits a behavior typical of all the junctions measured. On the basis of tunneling theory, one would expect the curve to be described by the cubic dependence of the form shown in the fourth-order expansion in Eq. (4). A computer program, FORLAN, was written to facilitate rapid calculation of the tunneling current as a function of the junction parameters. This program uses the complete analytical Forlani-Minnaja expression together with the near-linear (low-voltage) experimental values of I, V, and G_0 to determine the values of S for selected values of $\overline{\phi}$. The program can then generate full-range characteristic curves for different values of $\overline{\phi}$ so as to obtain a best fit to the experimental I-V curve.

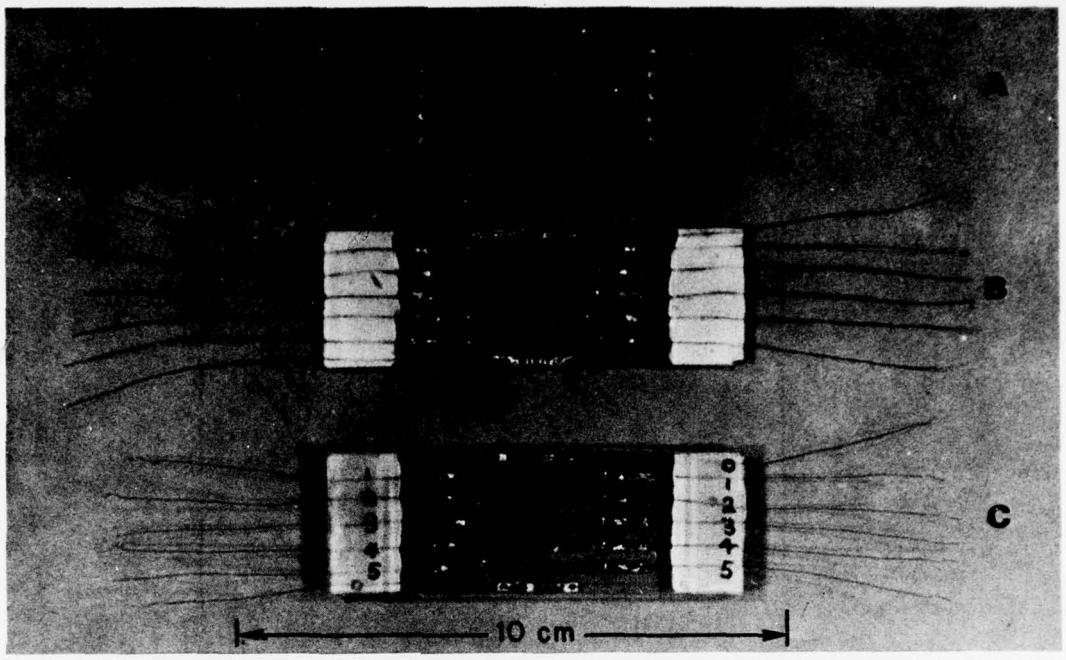

Fig. 5 — A typical assembly of five junctions shown at three stages of construction: (A) Pattern of indium contacts are attached to clean glass substrate. (B) Cross strip of aluminum is vacuum deposited and oxidized in pure oxygen at room temperature for $\approx$24 hours. (C) Finally, five parallel strips of aluminum are vacuum deposited at right angles to the cross strip to form five junctions.

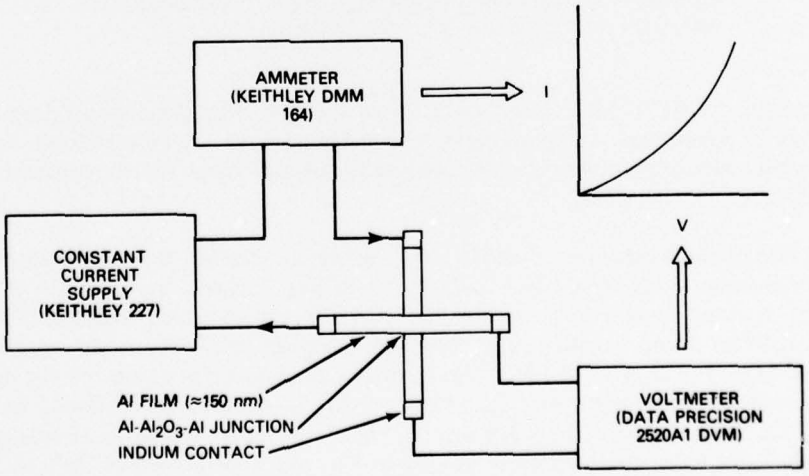

Fig. 6 — Standard four-point arrangement for measuring the current-voltage characteristics of the electron tunneling junctions

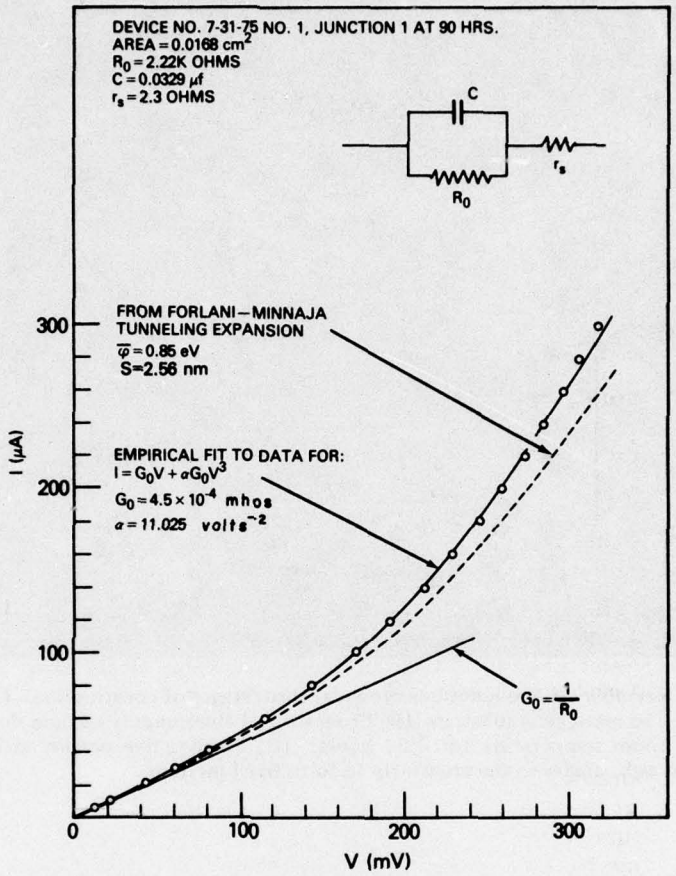

Fig. 7 — The current-voltage characteristic curve for a 0.0168-cm^2 junction measured 90 hours after fabrication. The equivalent circuit of the junction is shown in the upper right.

The quality of fit to the experimental data was found to vary, depending on the particular set of junctions. In some cases an excellent fit could be obtained, and in other cases the calculated curvature deviated substantially from the experimental data beyond 100 mV.

Using the best-fit values of S and $\overline{\phi}$, one can also calculate the tunneling current from the expansion in Eq. (4). The dashed line in Fig. 7 shows an example of such a calculation. It was found, however, that the current-voltage characteristics of all of the junctions could be fitted considerably better by using an empirical cubic equation of the form of Eq. (4): $I = G_0 V + \alpha G_0 V^3$. Here, when experimental values of G_0 and I and V at 100 mV and 200 mV were used, an average value of α could be obtained to give a satisfactory fit to the data. The solid line in Fig. 7 shows an example of this procedure. The α's calculated from the tunneling theory in Eq. (4) were generally 20% to 50% lower than the empirically determined α's. Since α is a measure of the nonlinearity and will later occur explicitly in the IM expression, we will use the empirical value of α as determined for each junction.

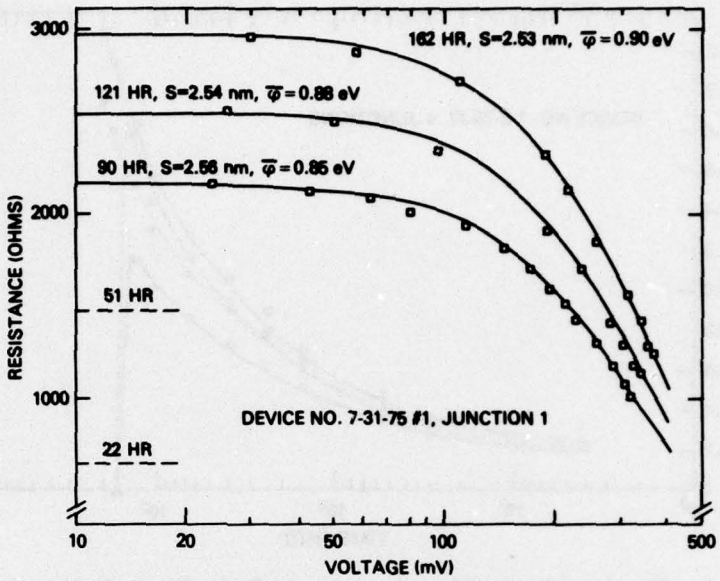

Fig. 8 — The behavior of junction resistance as a function of voltage and time. The solid curves are generated by the FORLAN program and represent a best fit to the experimental points for the indicated values of $\overline{\phi}$ and S.

It is also important to emphasize that the junction parameters G_0, α, $\overline{\phi}$, and S do not remain constant in time. As indicated, the characteristics shown in Fig. 7 were measured at 90 hours after fabrication. The junction resistance as a function of applied voltage for this same junction is shown in Fig. 8 with time as a parameter. Here the solid curves are a best fit to the experimental points using the FORLAN program. The curves show the sensitivity of the junction resistance to $\overline{\phi}$ and particularly to the insulator thickness S.

Although the marked change of resistance with time does not prevent the device from being well characterized, it does necessitate the additional inconvenience of keeping a time history of the individual junctions and of measuring the intermodulation within a few hours of any characteristic measurement. A time history of four typical junctions is shown in Fig. 9. These four junctions were fabricated simultaneously under the same conditions. The low-voltage resistance R_0 of each junction was tracked for 2000 hours or more. The intermodulation was generally measured from 6 to 48 hours after completion of fabrication. This time lapse was found to be convenient both because of the slow rate of resistance change and because the initial resistance (300 Ω to 3 kΩ) was more suitable for IM measurements.

An additional type of behavior that is characteristic of the junctions can be seen for two of the junctions, which self-shorted after about 1300 hours. Most of the junctions that were visibly free of fabrication defects lasted beyond a few hundred hours. In a few cases such shorts were observed to repair themselves (return to a resistance along the expected curve) following a voltage spike due to improper switching procedure. This

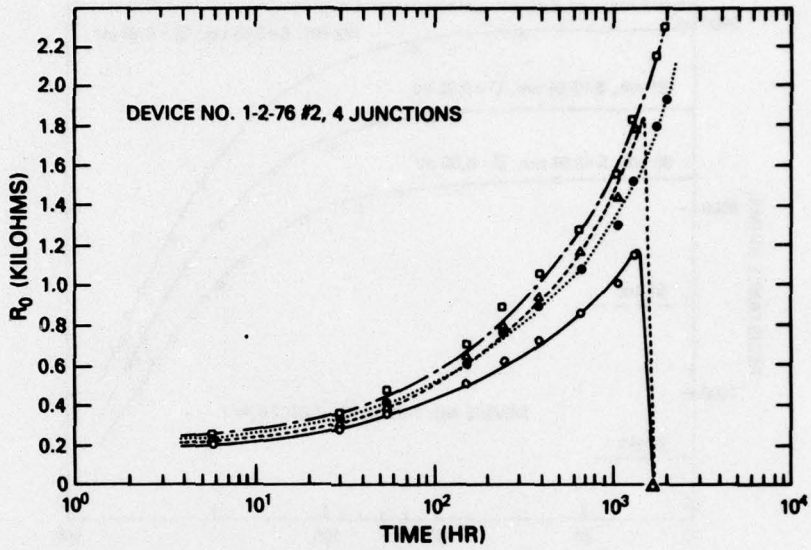

Fig. 9 — The time history of junction resistance R_0 for four typical junctions. The rate of resistance change increases continuously for several hundred to several thousand hours, followed usually by an abrupt self-shorting drop to fractions of an ohm.

behavior suggests the burnout of a localized filamentary short. The mechanism of the time-dependent behavior is not understood, but it appears to be due to a combination of diffusion at the interface, contaminant absorption, edge effects, and mechanical rupture [9]. However, all of the observed nonlinear and time-dependent behavior is assumed to realistically simulate the numerous microscopic tunneling points of real metal-to-metal contacts.

CAPACITANCE MEASUREMENTS

In addition to the nonlinear resistive characteristics of such junctions an important property which dominates the RF conduction is the junction capacitance. Although most of the junctions fabricated were of small area ($\lesssim 0.015$ cm^2), their capacitance is relatively large because of the small plate separation of $\approx$3 nm. The capacitances of the junctions were measured at 1.0 MHz with a Boonton direct capacitance bridge (Model 75D).

Since the thin-film device is not purely capacitive, the bridge will see the equivalent circuit of the device (Fig. 7). At balance the bridge and device admittances Y_B and Y_D respectively, or reciprocally the impedances, will be matched, so that $Y_B = Y_D$ and

$$Y_B = G_B + j\omega C_B. \tag{5}$$

Here the conductance G_B and capacitance C_B are read directly from the bridge. For the typical junction parameters shown in Fig. 7 and for frequencies $F \geq 1$ MHz, $R_0 >> X_C$, where $X_C = 1/2\pi fC$; therefore

$$Y_D \approx \frac{r_s}{r_s^2 + \dfrac{1}{\omega^2 C^2}} + j \frac{\dfrac{1}{\omega C}}{r_s^2 + \dfrac{1}{\omega^2 C^2}} . \tag{6}$$

By equating the real and imaginary parts of Eqs. (5) and (6), one can obtain the device capacitance C and series resistance r_s in terms of the bridge values G_B and C_B.

In using the value of capacitance thus determined one is assuming that the value of C is not a function of frequency or applied voltage. The value of C showed no measurable change with applied bias voltage up to 300 mV. Cursory experiments at audio frequencies also showed no frequency dependence of C. The use of a fixed value of C for the junction implies that the dielectric constant of the Al_2O_3 is not a function of voltage and that the capacitive part of the junction will conduct UHF linearly. A measurement of the capacitance also permits a determination of the effective plate separation of the junction sandwich. For a parallel-plate capacitor the separation S in nanometers is simply

$$S = 0.8854 \frac{KA}{C} , \tag{7}$$

where K is the dielectric constant for Al_2O_3, A is the plate area in cm^2, and C is the capacitance in μF. For the junction values shown in Fig. 7, $A = 0.0168$ cm^2 and $C = 0.0329$ μF. For a value of $K = 10.44$ [10], Eq. (7) gives a plate separation of 4.7 nm. This separation is considerably larger than either the 2.56 nm resulting from a parameter fit to the I-V characteristics (Forlani-Minnaja expansion in Fig. 7) or the 2.25 nm resulting from the digital thickness monitor measurements discussed in the previous section. This discrepancy has been observed by other investigators [11] and is believed to result from a different averaging process inherent in the different measuring techniques.

When IM effects are calculated, the bridge values of capacitance are used rather than the values calculated from tunneling or weight-gain measurements, since presumably the reactive RF current and voltages will behave in accordance with the effective value of C measured at 1.0 MHz. It will also be seen in the following section that the RF voltage developed across the resistive part of the junction is an extremely sensitive function of the capacitive reactance.

INTERMODULATION MEASUREMENTS

A block diagram of the basic IM test facility, together with the equivalent circuit of a tunneling junction, is shown in Fig. 10. Each transmitter power output can be varied independently from 0 to 100 W. The maximum third-order (290-MHz) intermodulation generated by the test facility alone is $\lesssim$-140 dBm at 50 dBm (100 W) total power output from the diplexer. The tunneling junctions under test are placed between the diplexer output and 150 m of RG-214 coaxial cable. The cable approximates an infinite transmission line and ideal termination [1]. In the case of the tunneling junction devices, the power levels were adjusted so that $P_1 = P_2$, and the total power input P_I to the junction was usually set to 1.0 W. The total power input of any device was kept below about 4 W because of the limited ability of the thin-film conduction strips to dissipate power.

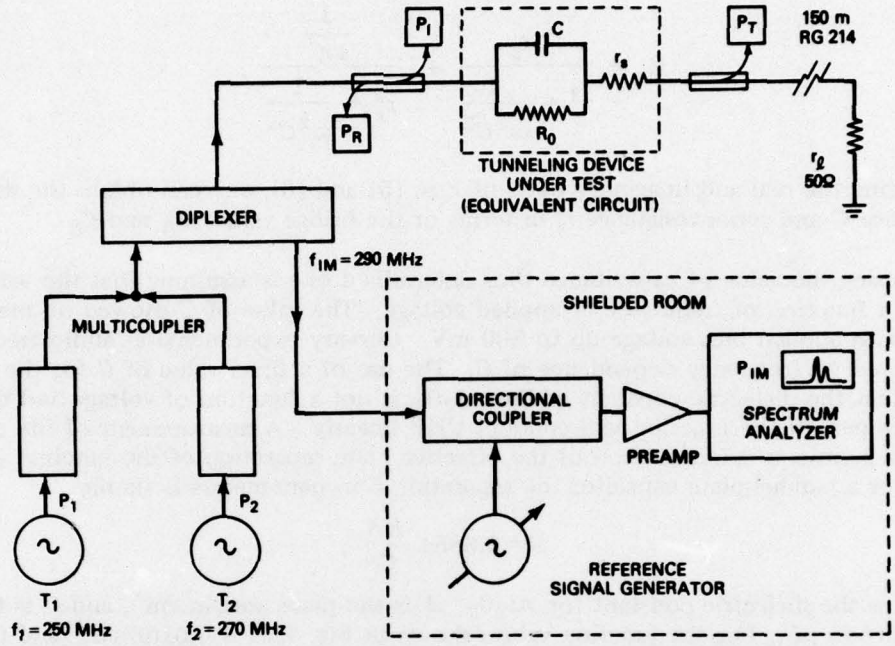

Fig. 10 — NRL intermodulation test facility (operated by the NRL Satellite Communications Branch). The equivalent circuit of a tunneling junction is shown in the normal test configuration.

As shown in Fig. 9, the junction resistance changes with time, making it necessary to measure the *I-V* characteristics just prior to IM measurements. Capacitance values are also measured prior to such IM test runs, even though the capacitance remains essentially constant with time. The resistance change with time, however, affords the opportunity to measure the intermodulation as a function of junction resistance.

The assembly of junctions, usually in a set of five as shown in Fig. 5, is mounted in a special chassis box (Fig. 11). To minimize the generation of spurious intermodulation, the aluminum chassis box contains no ferromagnetic materials and is fitted with low-IM type-N UHF connectors [1]. The IM power level of the chassis box was tested using a No. 14 bare copper shorting bar soldered between the terminals. These tests consistently showed IM levels of $\lesssim$-140 dBm at an input power of 1.0 W. One must also make sure that the thin-film structure associated with the junction assembly does not produce intermodulation. A measurement of this effect was made by using the film cross-strip on a set of five junctions as a shorting bar. At a 1.0-W input the IM level was measured at -140 dBm ± 5 dB. A thin-film strip, fabricated and mounted in the same way as the junction assemblies, also showed the same results. Therefore any intermodulation above the residual level of -140 dBm ± 5 dB would be due to the junction and not caused by the chassis box, connectors, or device structure external to the junction.

Because of the impedance mismatch of the chassis box to the 50-ohm coaxial cable, 45% of the power was observed to be reflected when using a copper shorting bar. When an assembly of junction devices is mounted in the chassis box, the transmitted power P_T drops from 55% to as low as 30%, depending on the size of the junctions. In most cases

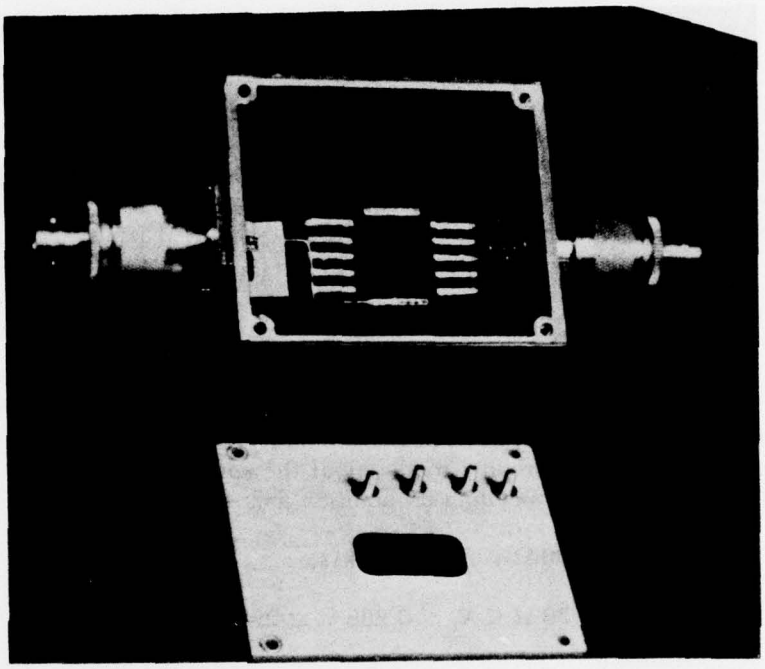

Fig. 11 — Junction assembly mounted in aluminum chassis box. Nonferromagnetic materials and low-IM type-N UHF connectors are employed to minimize spurious generation of intermodulation.

the impedance of the junction and leads is less than 20 Ω. The transmitted power P_T as experimentally measured is used in calculating the RF current passing through the junctions.

To calculate the IM power P_{IM} to be expected from a tunneling junction, we return to Eq. (2). For the tunneling junctions studied, it was found that the experimental DC current-voltage characteristics can be adequately described by

$$I = G_0V + G_2V^3. \tag{8}$$

In this case there is no V^2 term, since the tunneling current is essentially symmetric about the origin of the I-V characteristics. Also, as can be seen from Eq. (3), any V^2 term would produce no IM frequencies falling within the receive band. Equation (8) can be written in a more convenient form by letting $\alpha = G_2/G_0$, so that

$$I = G_0V + \alpha G_0V^3, \tag{9}$$

where G_0 is the usual linear conductance and α is a ratio that measures the departure from linearity. In the case of an RF input voltage of the form of Eq. (1), the current in Eq. (9) can be written as shown in Eq. (3), except that here only the experimentally observed angular frequencies ω_1, ω_2 and $2\omega_2 - \omega_1$ are retained:

$$I(t) = G_0(V_1 \cos \omega_1 t + V_2 \cos \omega_2 t) + \frac{3}{4} \alpha G_0 V_1 V_2^2 \cos (2\omega_2 - \omega_1)t$$
$$= I_0(t) + I_{IM}(t). \tag{10}$$

It is important to note that $I(t)$ is the RF current through the nonlinear resistance R_0, that $I_0(t)$ is the primary current at frequencies f_1 and f_2, and that $I_{IM}(t)$ is the intermodulation current at frequency $2f_2 - f_1$. The peak IM current is just

$$I_{IM(peak)} = \frac{3}{4} \alpha G_0 V_1 V_2^2. \tag{11}$$

The value of V_1 and V_2 can be calculated from the total transmitted power P_T. The transmitted power P_T results from both power inputs P_1 and P_2 running simultaneously at frequencies f_1 and f_2. The circuit parameters of the equivalent circuits in Figs. 7 and 10 have the following ranges, depending on junction area and history:

$$300\ \Omega < R_0 < 100\ \text{k}\Omega,$$

$$0.026\ \Omega < X_c < 0.296\ \Omega \text{ at } 290\ \text{MHz},$$

$$2\ \Omega < r_s < 25\ \Omega,$$

$$r_\ell = 50\ \Omega.$$

For all cases $R_0 >> X_c$, so that essentially all of the transmitted current I_T ($I_T(t) = I_1 \cos \omega_1 t + I_2 \cos \omega_2 t$) passes through the capacitance C and the total transmitted power P_T is dissipated in the series resistance r_s and the load resistance r_ℓ. Since $r_s + r_\ell$ determines the current, the measured RF power P_T is

$$P_T = \langle I_T^2(t) \rangle (r_s + r_\ell), \tag{12}$$

where

$$\langle I_T^2(t) \rangle = \frac{1}{T} \int_0^T (I_1 \cos \omega_1 t + I_2 \cos \omega_2 t)^2 \, dt.$$

For $P_1 = P_2$ and $I_1 = I_2$, Eq. (12) yields

$$I_{T(peak)} = \left[\frac{P_T}{r_s + r_\ell}\right]^{1/2}.$$

Since essentially all of this current passes through the capacitance, the voltages V_1 and V_2 developed across the capacitance C and also across the nonlinear resistance R_0 are approximately

$$V_1 = X_{C1}\left[\frac{P_T}{r_s + r_\ell}\right]^{1/2} \text{ and } V_2 = X_{C2}\left[\frac{P_T}{r_s + r_\ell}\right]^{1/2},$$

where X_{C1} and X_{C2} are the capacitive reactances at f_1 and f_2. With these values of V_1 and V_2, Eq. (11) becomes

$$I_{IM(peak)} = \frac{3}{4}\,\alpha G_0\left[\frac{P_T}{r_s + r_\ell}\right]^{3/2} X_{C1}X_{C2}^2. \tag{13}$$

This IM current is viewed as being generated in the nonlinear element R_0, and, as can be seen from Fig. 10, this current source is paralleled by the junction capacitance C and the external load $r_s + r_\ell$. Again $X_C \ll r_s + r_\ell$ at 290 MHz, so that most of this current is shunted through C, and the voltage developed across C and also across the external load $r_s + r_\ell$ is

$$V_{IM(peak)} = I_{IM(peak)}X_{C,IM}, \tag{14}$$

where $X_{C,IM}$ is the capacitive reactance at 290 MHz. The IM power dissipated in $r_s + r_\ell$ is then

$$P_{IM} = \frac{< V_{IM(peak)}^2 \cos^2 (2\omega_2 - \omega_1)t >}{r_s + r_\ell} = \frac{1}{2}\,\frac{V_{IM(peak)}^2}{r_s + r_\ell}. \tag{15}$$

Combining Eqs. (13), (14), and (15), we obtain finally

$$P_{IM} = \frac{9}{32}\,\alpha^2 P_T^3\,\frac{X_{C1}^2 X_{C2}^4 X_{C,IM}^2}{R_0^2(r_s + r_\ell)^4}. \tag{16}$$

This equation expresses the IM power level in terms of readily measurable junction and test parameters. The RF test facility is set up to measure the IM power level in dBm units (decibels referenced to 1 mW), so that by definition Eq. (16) can be expressed as

$$(\text{dBm})_{IM} = 10 \log \frac{P_{IM}\ (\text{watts})}{10^{-3}\ (\text{watts})}. \tag{17}$$

This dBm level of intermodulation is measured directly at the spectrum analyzer by comparison to a reference signal, as shown in Fig. 10.

The junctions initially measured in the IM test facility had relatively large areas ($A \gtrsim 0.015\ \text{cm}^2$) and were operated at an input power of ≈ 1.0 W. For a transmitter power $P_T = 0.5$ W these junctions showed intermodulation levels of -110 to -135 dBm, depending on the values of R_0 and C of the particular junction. Figure 7 shows the *I-V* characteristics and parameters typical of this type of junction. If one uses the values shown in Fig. 7 together with $P_T = 0.5$ W and $R_\ell = 50\ \Omega$, a calculation of the IM power from Eq. (16) gives a much lower IM level of -239 dBm.

In the preceding calculation it was assumed that the RF current is uniformly conducting through the film strip and junction area. At input frequencies of 250 and 270 MHz, however, one might expect UHF skin effects to significantly alter the IM level. An accurate calculation of the RF current distribution and resultant intermodulation is an extremely complex problem for the geometry of the thin-film junction device.

One simplifying approximation, which has been employed by Chapman et al.[2] regarding waveguide flanges, is to restrict the RF current across the tunneling area to the same depth as the skin depth in the adjacent conductor. Although the geometry of a thin-film device differs significantly from a comparatively large flange, a similar restriction arises through edge concentration of RF current in thin-ribbon conductors. (Evidence of such a current distribution was indicated in one set of junctions in which the RF power had exceeded 10 W. Small thermally produced blisters showed a marked concentration along the outer edge of the conducting strips.)

For this approximation the effective RF current is restricted to an average skin depth of $\approx 5.16 \times 10^{-4}$ cm around the perimeter of the actual junction area. For the junction parameters shown in Fig. 7, the effective RF conduction area is 2.67×10^{-4} cm^2, or about 1/63 the apparent area. Thus the effective junction resistance and capacitance become $\approx 1.39 \times 10^5$ Ω and $\approx 5.23 \times 10^{-10}$ F respectively. With these effective values of R_0 and C, Eq. (16) gives an intermodulation level of -131 dBm, which is within the experimental range observed.

To raise the IM level and to examine any area effects, several sets of five-junction assemblies were fabricated in graded sizes ranging from 0.015 cm^2 down to 0.0015 cm^2. It was found that the size scaling effect on capacitance C and junction resistance R_0 essentially followed the expected variation for such junction elements in parallel. As the junction area is decreased, one would expect, according to Eq. (16), the capacitive reactance product ($X_{C1}^2 X_{C2}^4 X_{C,IM}^2 \approx X_{av}^8$) to increase much faster than R_0^2 and to result in a rapid increase in P_{IM} with decreasing area. This increase is largely offset, however, by an increase in the ratio of effective RF conduction area to total junction area as the junction area decreases. When the present fabrication techniques are used, a reduction in junction area by more than an order of magnitude becomes impractical, and the power-handling ability becomes too low to conveniently make IM measurements.

Figure 12 shows typical results of IM measurements on a set of five junctions ranging in size from 0.0143 cm^2 to 0.0018 cm^2. The measured value of the junction capacitance, is shown along the abscissa. The IM power level in dBm units and in watts is shown on the left and right ordinates respectively. The input power P_I is held constant at +30 dBm (1.0 W). Over the capacitance range examined the transmitted power P_T varies from 0.39 W to 0.51 W but remains relatively constant on the scale shown. The IM level for each junction is plotted as a square point along with the estimated error bars of ±3 dB. These experimental points are connected with a smooth dashed curve. The solid curve shows the intermodulation calculated from Eq. (16) using the experimentally measured junction parameters with the values of R_0 and C corrected to the effective RF skin depths. The uncorrected junction parameters are shown in Fig. 13. Similar sets of junctions showed the same functional dependence of intermodulation on area and capacitance as illustrated in Fig. 12.

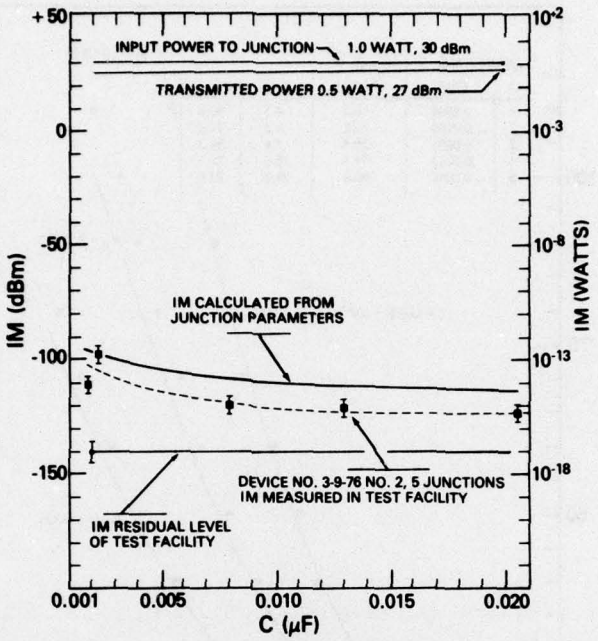

Fig. 12 — Experimental and calculated intermodulation power levels generated by electron tunneling as a function of junction capacitance. Here the variation in capacitance results from a gradation in junction areas ranging from 0.0018 cm^2 to 0.0143 cm^2. All junctions were fabricated simultaneously and have the same oxide thickness of $\approx$2.5 nm. The junction parameters and *I-V* characteristics for each of the five junctions are shown in Fig. 13.

Although the intermodulation calculated in the preceding manner followed the experimental variation with junction parameters fairly well, the absolute magnitude of the calculated IM curve was found to be shifted from the measured intermodulation by ±15 dB. This agreement is perhaps as good as can be expected in view of the crude RF skin-depth approximations used. Additional smaller effects which are not taken into account by Eq. (16) are distributed resistance and capacitance effects, nonlinear capacitive effects, and frequency-dependent effects.

The equivalent-circuit analysis leading to Eq. (16) tacitly assumes that the film resistance r_f over the junction area is zero. Actually this resistance is generally larger than the capacitive reactance at 270 MHz; for example, in junction 1 of Fig. 13, X_C = 0.0286 Ω and r_f = 0.185 Ω. Thus, one should consider the effects of distributed resistance and capacitance along the junction area. With use of a two-dimensional model, both an exact continuous-distribution analysis and a numerical discrete analysis showed a voltage distribution $V(x)$ that varied significantly along the width of the junction. In addition the RF edge conduction along the film strip leading up to the junction area will increase the effective value of r_s. A calculation of these two combined effects for junction 1 of Fig. 13 using a discrete four-segment equivalent circuit yielded a value of P_{IM} which differed from the previously corrected value by only 1 dB. However, this small net

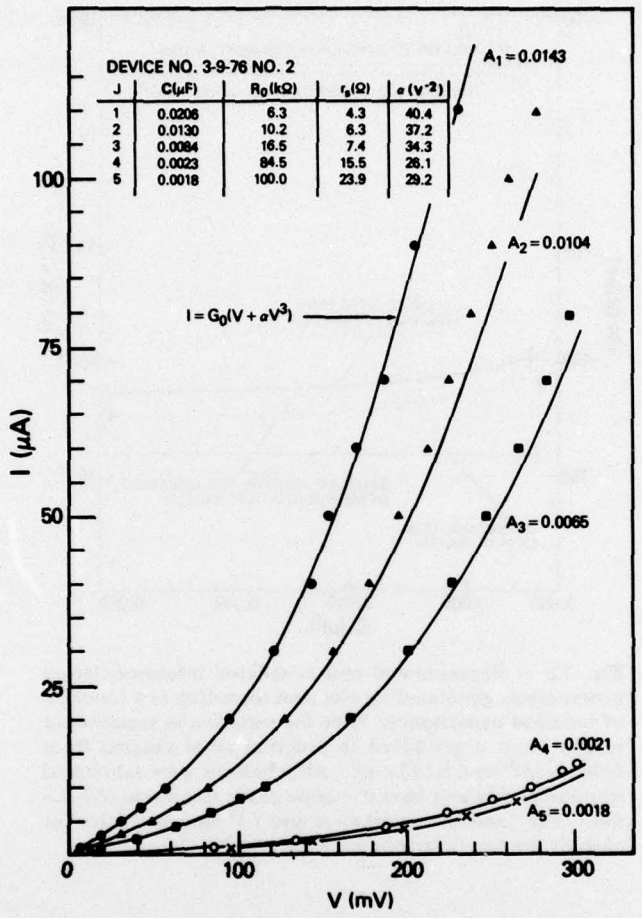

Fig. 13 — Current-voltage characteristics as a function of area and capacitance for the five junctions measured in Fig. 12. The corresponding junction parameters are shown in the upper-left table.

correction is due to the fortuitous approximate cancellation of the two effects for the geometry chosen.

The α of Eq. (16) is derived from the nonlinear DC resistance characteristics of the junction. This nonlinearity is presumed to arise solely from electron tunneling, as described previously. However, known nonlinear capacitance effects can arise through nonlinear dielectric and electrostriction effects [12]. Electrostriction can also change the tunneling resistance through a volume change. A rough calculation of the volume-change effect predicted an intermodulation well below the level of detectability.

Equation (16) is also applied to RF power measurements of P_{IM} and P_T in the UHF range (240 MHz to 290 MHz), whereas the parameters α, R_0, and r_s are determined from DC measurements and C is measured at 1 MHz. The assumption of frequency

independence seems reasonable, since the resistivity and dielectric constant of Al_2O_3 appear to be relatively constant over a wide range of frequencies [13,14].

ION IMPLANTATION EFFECTS

To eliminate or reduce the IM effects of tunneling junctions in metal-to-metal contacts, one apparently must either eliminate the surface insulating films (oxides or otherwise) or basically modify the structure of the metal oxide surface. Fabrication of full-scale metal hardware that is essentially free of metal oxide films both at the surfaces and under metal platings such as gold would appear to offer a reasonable solution. Alternatively, modification of the metal oxide surfaces should ideally make any contacts more conductive, linear, and free of time-dependent effects. We have explored implantation of metallic ions in the oxide surface as a possible way to achieve the desired results.

Several tunneling junctions were fabricated similarly as previously described, except Ag^+ ions of ≈ 2 keV energy were implanted into the Al_2O_3 surface prior to the evaporation of the second overlapping aluminum strip. Theoretical estimates indicate that 2-keV Ag^+ ions have a mean range in Al_2O_3 of ≈ 1.7 nm. Ideally these silver atoms will have a Gaussian distribution about the mean range with a standard deviation of ≈ 0.6 nm. A plot of Gaussian distribution shows range straggling extending from the surface to ≈ 3.2 nm, with about 12% of the silver atoms stopping in the aluminum beyond the Al_2O_3.

The actual distribution of the silver atoms in the Al_2O_3 and Al may be quite different than just described because of three effects that have not been measured:

- Uncertainty in the low-energy range of Ag^+ ions in Al_2O_3 (existing data indicate that heavy-ion ranges in light substrates may be as much as twice the theoretical estimates),
- Removal of the Al_2O_3 surface by ion sputtering, and
- Oxide regrowth when the film is removed from the vacuum environment.

To evaluate the electrical characteristics of such implanted junctions, standard reference monitor junctions were also fabricated simultaneously on the same substrate and under the same conditions without ion implantation. All electrical measurements are then referenced to the monitor junctions. This procedure is necessary because different batches of junctions will generally have different values of R_0 and because the electrical characteristics will be measured at different times.

Initially two sets of junctions (three reference junctions per set) were implanted. One set was implanted with a fluence of $\approx 10^{15}$ atoms/cm^2, and the other set was implanted with a higher fluence of $\approx 10^{16}$ atoms/cm^2. The junction implanted at the higher fluence showed a sharp drop in resistance from an average resistance of 36.3 kΩ to an average resistance of 13.5 Ω, or a ratio of implanted resistance R_0(Ag) to reference resistance R_p(Ref.) of $\approx 4 \times 10^{-4}$. The junctions implanted at lower fluence, however, unexpectedly showed an increase from 12.3 kΩ to 23 MΩ, or a ratio $R_0(Ag)/R_0(Ref.) = 1.9 \times 10^3$. The different implant fluences produced opposite effects of change in resistance that differed by over six orders of magnitude!

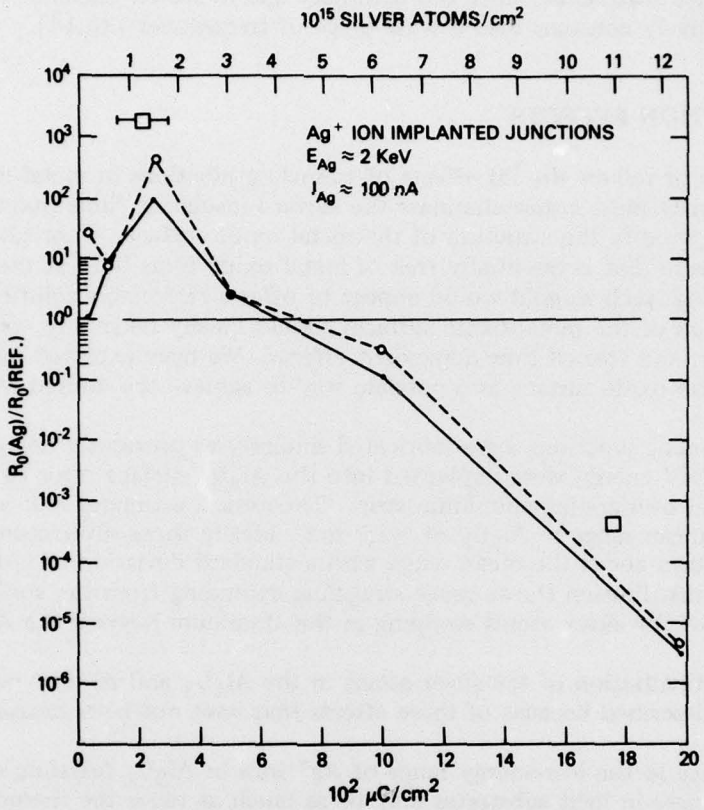

Fig. 14 — Effect on junction resistance of implantation of 2-keV silver ions in the Al_2O_3 surface as a function of fluence of silver atoms. The ratio of ion-implanted resistance R_0(Ag) to an identical unimplanted resistance R_0(Ref.) is plotted on the ordinate.

In view of this surprising result a more elaborate set of junctions were fabricated to facilitate measurement of the junction resistance as a function of the fluence of silver atoms implanted. Figure 14 shows the results of these measurements. The ratio R_0(Ag)/R_0(Ref.) is plotted on the ordinate, and the fluence of silver atoms and of charge are plotted along the top and bottom abscissa respectively. The solid line connects points measured immediately after fabrication, and the dashed line connects points measured about 2 hours later. The resistances are changing rapidly during this initial period, but the ratio remains relatively constant in time. The two square points are from the original measurements and are seen to be consistent with the more detailed later results. The error bar on one square point is significantly higher than the errors for the other points and resulted from an equipment-produced uncertainty in the charge fluence at this one point. The increase in junction resistance for implants up to $\approx 4 \times 10^{15}$ atoms/cm^2 was completely unexpected, and the detailed physical mechanisms responsible for the functional behavior of R_0(Ag)/R_0(Ref.) with the silver implant fluence are not yet fully understood. Recent work [15] shows that ion implantation in the oxide surface of metals has the effect of increasing the oxide thickness. This effect would account

for the initial increase in tunneling resistance. As the silver density is increased, the oxide conductivity apparently increases faster than the competing thickness-growth, resulting in a low-resistance junction. For those junctions implanted to fluences of $\geqslant 10^{16}$ atoms/cm^2 the resistance R_0 was generally reduced to a few ohms or fractions of an ohm. The current-voltage characteristics of the implanted junctions showed better linear behavior than unimplanted junctions over the same current range. Although these junctions had greatly improved conduction characteristics, they continued to show the familiar time-dependent increase of R_0.

Preliminary test of these junctions at the IM test facility confirmed that the low-resistance implanted junctions did indeed have a low intermodulation of $\approx$-135 dBm. For such an implantation technique to be useful on full scale hardware, however, one would have to solve the formidable problems of the time-dependent behavior and mechanically fragile surfaces.

CONCLUSIONS

From our experimental and theoretical investigation of the generation of intermodulation by electron tunneling in Al-Al_2O_3-Al junctions, we list the following conclusions:

- Tunneling junctions ranging in areas from $\approx$0.015 cm^2 down to $\approx$0.0015 cm^2 showed IM levels of $\approx$150 dB to $\approx$110 dB below the total transmitted power of 0.5 W. This corresponds to a P_{IM}/P_{sig} ratio of 10^{-15} to 10^{-11} respectively. Since ideally the ratio P_{IM}/P_{sig} should be $\lesssim 10^{-19}$, the electron tunneling mechanism is seen to be a significant source of intermodulation.

- The functional dependence of the IM power on the effective RF junction parameters appears to be satisfactorily described by Eq. (16).

- Although the main features of the current-voltage characteristics of the junctions are described by the Forlani-Minnaja theory, an accurate fit to the experimental data was not always possible over the entire range of experimental values.

- No significant effects of hysteresis in the *I-V* characteristics were observed. However, a small resistance asymmetry was always observed at the higher voltages. If the film strip oxidized first was operated at a positive polarity, the junction resistance was lower than the reverse polarity by 3% to 7%. Thus the junctions exhibit a small rectifying component that is thought to arise from the asymmetry of the Al_2O_3 density profile at the two interfaces.

- In well-characterized Al-Al_2O_3-Al junction devices the time-dependent behavior is prominent, with the junction resistance increasing continuously for several hundred to several thousand hours, followed usually by an abrupt self-shorting drop to fractions of an ohm. During such resistance increase, the capacitance remains essentially constant. Such time-dependent behavior is assumed to take place randomly in the numerous microscopic tunneling points in real hardware contacts. This is a mechanism that could contribute to the erratic fluctuation of intermodulation observed in macroscopic contacts.

• Ion implantation of $\gtrsim 10^{16}$ silver atoms per cm^2 in the oxide surfaces produced low-resistance and low-IM junctions but failed to stop the characteristic increase of junction resistance with time. Our initial implantation results are sufficiently promising, however, to warrant further investigation of the possible beneficial effects of employing different metallic-ion species, greater implantation depths, and higher fluences.

ACKNOWLEDGMENTS

The work presented in this report was supported by the Naval Electronic Systems Command and represents a part of a larger NRL intermodulation program under the direction of Dr. V. J. Folen of the Materials Sciences Division. The authors are indebted to Dr. Folen for his support and project management throughout this investigation.

We are also particularly indebted to Dr. B. J. Faraday, Head of the Radiation Effects Branch, for his continuous guidance and assistance in addressing the various problems in all phases of the work.

We express special appreciation to Mr. Charles F. Young of the Satellite Communications Branch for his thorough and patient accommodation of the authors' numerous requests during device-testing at the intermodulation test facility.

We thank Dr. J. K. Hirvonen of the Materials Modification and Analysis Branch for his able consultation and assistance during the ion implantation experiments and also for the generous allocation of beam time on the newly installed ion implantation facility.

We thank Dr. Warren L. Bendel of the Radiation Effects Branch for a thorough review of the manuscript and for making important corrections to our analysis.

We also express an appreciation to Mr. Edwin P. Westbrook of the Radiation Effects Branch for his help on RF analysis problems during numerous consultations.

REFERENCES

1. C.E. Young, "The Danger of Intermodulation Generation by RF Connector Hardware Containing Ferromagnetic Materials," National Electronic Packaging Conference, 76-West Connector Symposium/Proceedings, Anaheim, Calif., Feb. 23-26, 1976, and "An Update on Intermodulation Generation by RF Connector Hardware Containing Ferromagnetic Materials," Ninth Annual Connector Symposium Proceedings, Cherry Hill, N.J., Oct. 20-21, 1976.
2. R.C. Chapman, J.C. Darlington, A. Savarin, R. Steinberg, A. Paul, and R. Moss, "Intermodulation Generation in Normally Passive Linear Components," Philco-Ford Corporation Report WDL-TR5242, Aug. 24, 1973.
3. W.H. Higa, *Proc. IEEE* 63, 306 (1975).
4. C.B. Duke, *Tunneling in Solids*, Academic Press, New York, 1969, p. 60.
5. F. Forlani and N. Minnaja, *Il Nuovo Cimento* 31, 1246 (1964).
6. C.S. Guenzer, *Proc. IEEE* 64, 283 (1976).

7. R. Stratton, *J. Phys. Chem. Solids* 23, 1177 (1962).

8. W.F. Brinkman, R.C. Dynes, and J.M. Rowell, *J. Appl. Phys.* 41, 1915 (1970).

9. C.S. Guenzer, C.D. Bond, and C.A. Carosella, *Bull Am. Phys. Soc. II*, 21, 273 (1976).

10. AIP Handbook, 2nd edition, McGraw-Hill, 1963, p. 9-93.

11. K.H. Gundlach and G. Heldmann, *Solid State Communications* 5, 867 (1967).

12. G.H. Stauss, "Intrinsic Sources of IM Generation," unpublished NRL study report, NRL Code 6451, 1976.

13. G.V. Samsonov, *The Oxide Handbook*, IFI/Plenum, 1973, p 266 and 315.

14. H.P. Westman and J.E. Schlaikjer, *Reference Data for Radio Engineers*, ITT Corp., 1962, pp. 62 and 63.

15. V. Ashworth, D. Baxter, W.A. Grant, and R.P.M. Procter, *Corrosion Science* 16, 775 (1976).